

Optimal Control for X-Ray Microscopes

Sheikh T. Mashrafi , Member, IEEE, Junjing Deng, Curt Preissner, and Srinivasa M. Salapaka , Senior Member, IEEE

Abstract—In this article, a systematic framework for designing the control for fine positioning (scanning) stages of X-ray microscopes is presented. This framework facilitates designs that simultaneously achieve specifications on positioning resolution and tracking bandwidth while guaranteeing robustness of the closed loop device to unmodeled uncertainties. We use robust optimal control techniques for modeling, quantifying design objectives and system-specific challenges, and designing the control laws. The control designs were implemented on a three degree of freedom piezoactuated flexure stages dedicated for fine positioning of X-ray optics. Experimental results demonstrate significant improvements in positioning performance of 134%, 150%, and 132% in tracking bandwidths along the lateral (X), vertical (Y), and beam (Z) directions, respectively, when compared to proportional-integral-derivative controller designs. This was achieved while keeping similar or better positioning resolution and robustness measures. Fast scanning for X-ray imaging was demonstrated in both the step scan and flyscan modes, where bandwidth was improved by over 450 times with flyscan compared to the step scan.

Index Terms—Disturbance rejection, nanopositioning system, noise attenuation, positioning resolution, robust control, tracking bandwidth, X-ray microscope.

I. INTRODUCTION

X-RAY microscopy has a dramatic impact on different fields, as diverse as biological and life science, geo/soil science, environmental science, polymer science, physics, and chemistry. The high spatial resolution (30 nm or better) and the

Manuscript received July 23, 2019; revised November 20, 2019 and January 26, 2020; accepted January 28, 2020. Date of publication February 17, 2020; date of current version April 15, 2020. Recommended by Technical Editor Q. Zou. This work was supported in part by the U.S. Department of Energy, Office of Science, Office of Basic Energy Sciences, under contract DE-AC02-06CH11357 and DOE STTR Grant DE-SC0004283, in part by DOE Argonne National Laboratory under Grant 4J-30401-0007A, and in part by the National Science Foundation Civil, Mechanical and Manufacturing Innovation under Grant 14-63239. (Corresponding author: Srinivasa M. Salapaka.)

Sheikh T. Mashrafi was with the Department of Mechanical Science and Engineering, University of Illinois at Urbana-Champaign, Urbana, IL 60801 USA. He is currently with the Advanced Photon Source, Argonne National Laboratory, Lemont, IL 60439 USA (e-mail: mashrafi@anl.gov).

Junjing Deng and Curt Preissner are with the Advanced Photon Source, Argonne National Laboratory, Lemont, IL 60439 USA (e-mail: junjingdeng@anl.gov; preissner@anl.gov).

Srinivasa M. Salapaka is with the Department of Mechanical Science and Engineering, University of Illinois at Urbana-Champaign, Urbana, IL 60801 USA (e-mail: salapaka@illinois.edu).

Color versions of one or more of the figures in this article are available online at <http://ieeexplore.ieee.org>.

Digital Object Identifier 10.1109/TMECH.2020.2974318

high penetration of samples (10–100 μm) enable measurements not accessible with either electron or scanning probe microscope [6], [20], [23], [25] or X-ray microscope [9], [11]. The X-ray microscope is a well-established tool at the third-generation synchrotron facilities (APS, NSLS-II, ESRF, SPring-8, PETRA-III), which are particle accelerator systems where intense and partially coherent beams of X-rays are produced by passing electron beam through special magnet arrays and the insertion devices. Recent developments in accelerator technology are enabling improved electron beam qualities, with a dramatic 100-time improvement in the brightness of the resulting X-ray beam [12]. The improved brilliance and higher coherent fraction of X-rays from these new accelerators have the potential to improve the performance of X-ray microscopes by allowing for a higher resolution, shorter experiment times, and higher efficiency. X-ray optics is also continuing to improve for a finer focused beam and it is reasonable to expect the advent of optics capable of focusing below 10 nm. For scientific users to take full advantage of the combined improvements in the X-ray beam and optics, a commensurate improvement in the instrumentation engineering of the X-ray microscope is needed. Specifically, a significant performance enhancement can be achieved by making substantial changes to the control approach for the X-ray optics fine scanning stages. The motion control of the optics scanning stages will result in better closed-loop tracking bandwidth and high positioning resolution, which in turn will result in higher spatial resolution of the X-ray image and imaging speed. In this article, we present a new control architecture for fine positioning of X-ray microscope optics scanning stages that offers significant improvements over the state of the art in tracking bandwidth, positioning resolution, disturbance rejection, and noise attenuation.

Scanning transmission X-ray microscopy (STXM) is a high spatial resolution imaging technique, where the X-ray beam is focused into a small spot (100 nm or less) on the sample, which is then scanned on the sample plane orthogonal to X-ray beam to obtain an image. The image is postprocessed from the intensity of the transmitted X-rays that is recorded by an area photon detector placed downstream of the sample. The microscope spatial resolution is determined both by focus of the X-ray optics and the relative position stability between optics stage and the sample stage. Any relative motion between the optics and the sample, except the predefined reference trajectory, manifests as a larger focused X-ray spot on the sample and subsequent reduced X-ray image spatial resolution.

In this article, our controller design concentrates on a STXM optics scanning system (15 and 10 μm motion range in X and

Y direction, respectively), which provides motion as small as 10 nm. Ptychographic microscopes that combined STXM and coherent diffraction imaging [19], [22] and scanning X-ray fluorescence microscopy can also take advantage of better positioning resolution and trajectory control. Typically, high-resolution positioning systems in X-ray microscopes comprise piezoactuated, high-stiffness flexure stages. The main challenges in designing control laws for such systems arise from the limitations imposed by structural dynamics, modeling uncertainties (including environmental disturbances, parameter variations, and piezo nonlinearities), and noisy measurements, the combined effects of which severely limit the positioning performance. X-ray microscopy applications demand high specifications on performance such as: nanometer-scale positioning resolution, closed-loop bandwidths that are close to the flexure-stage resonant frequencies, millimeter-scale travel range, and repeatability, all in the presence of unmodeled uncertainties.

State-of-the-art fine-motion stages in X-ray microscopes typically use proportional–integral–derivative (PID) control, PID augmented with various types of filters, and some feed forward control methods. These model-independent architectures, while easily available as commercial motion control hardware, have limited ability to address limitations of the mechanics, actuators, and motion controller; in many cases these architectures are ill suited to low-damped systems such as the flexure stages [25]. Our approach is a means to directly address these limitations in a way not previously used in the context of X-ray microscope. While some authors have brought the small form-factor concept of scanning probe microscopy (SPM) to the realm of the X-ray microscope [19], no one to our knowledge has applied the tools of modern control design for fine-motion control to the X-ray microscope application as has been done in SPM applications.

In our framework, we use robust optimal control methods for designing control feedback laws. Here an optimization problem is posed and solved, which incorporates multiple performance objectives, which include high-tracking bandwidth, high positioning resolution, robust tracking of reference signals, disturbance rejection and measurement noise attenuation, and bounded control effort to ensure feasibility of implementation. The approach determines if a given set of specifications are feasible, and when they are, it yields an optimal control law. It also allows a designer to make tradeoffs between positioning resolution, tracking bandwidth, and robustness. These tools open the possibility of optimizing the performance of an X-ray microscope for specific applications and desired specifications by managing the tradeoff between the positioning resolution and the reference tracking bandwidth while simultaneously limiting the influence of unmodeled uncertainties such as environmental noise, for instance optimizing high-tracking bandwidth for step scanning and fly scanning or high positioning resolution for fluorescence microscopy.

II. VELOCIPROBE X-RAY MICROSCOPE

The Velociprobe (Fig. 1) is a next-generation X-ray microscope, which is built at Advanced Photon Source (Argonne National Laboratory) to enable ultrahigh-resolution X-ray

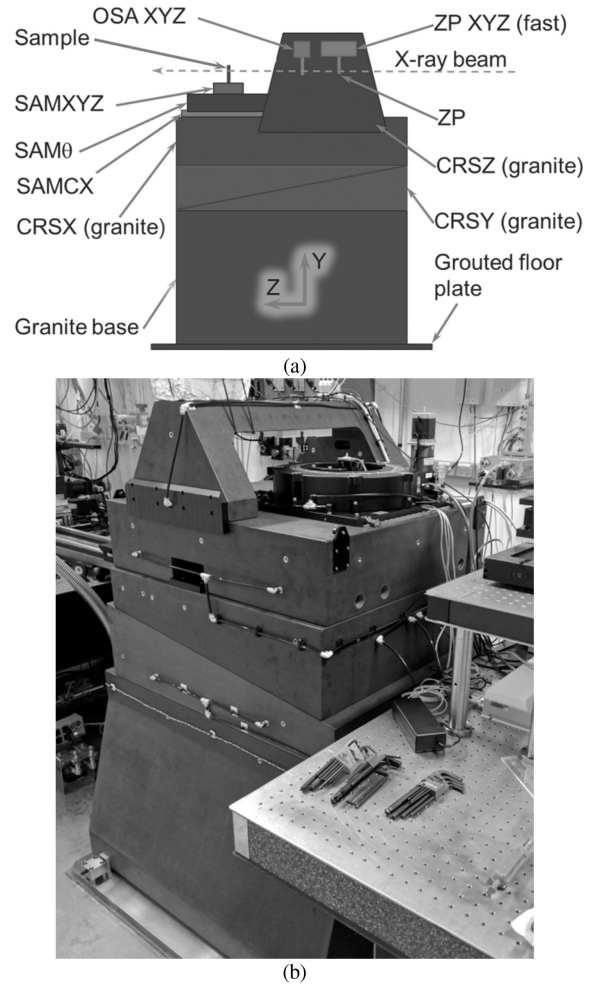


Fig. 1. (a) Schematic of the Velociprobe X-ray microscope. The coarse stages are made of large granite blocks, which are given motion utilizing state-of-the-art air bearing. The fine positioning zone plate XYZ stages, attached to the top granite gantry in an inverted orientation, is used to do high-precision scanning of the focused X-ray spot to cover a target area on the sample. (b) Installed instrument at APS Sector 2 beamline.

imaging in an ultrastable microscope platform and to complement the APS-U. It consists of a novel in-house coarse positioning stage, a state-of-the-art commercially available optics scanning nanopositioning stages (ZP XYZ), sample coarse positioning stages (SAM XYZ), and sample rotation stages (SAM θ). The coarse positioning stages are made of granite, which provides coarse motion utilizing integrated air bearings. During X-ray imaging, the coarse positioning granite stages remain static and the air bearings that support the granite blocks are vented. This makes the granite base, coarse positioning Y stages (CRSY), coarse positioning X stages (CRSX), and coarse Z positioning granite gantry (CRSZ) on top, act as one granite block. This results in minimal amplification of environmental disturbance, very low relative motion between the optics and sample, and results in an ultrastable platform for X-ray microscopy. The zone plate optics scanning stage assembly (ZPXYZ) is attached to the top gantry in an inverted manner to satisfy the working distance constraint between the zone plate optics and the sample.

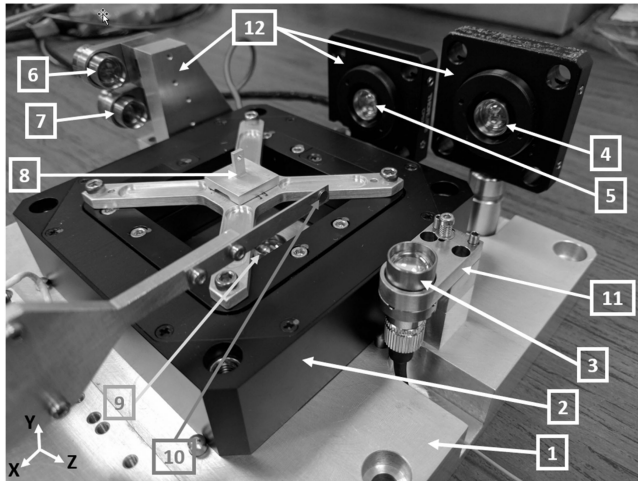


Fig. 2. Velociprobe fine scanning optics stage assembly. 1 = reference frame, 2 = PI stages, 3 = sensor sample Y-axis, 4 = sensor sample X-axis, 5 = sensor optics X-axis, 6 = sensor sample Z-axis, 7 = sensor optics Z-axis, 8 = optics kinematic holder, 9 = sensor optics Y-axis, 10 = order sorting aperture, and 11 and 12 = fixtures that hold the sensors.

Fig. 2 shows the fine positioning optics stage assembly (ZP XYZ) of the Velociprobe X-ray microscope on a table setup, before being assembled on to the Velociprobe granite gantry CRSZ (Fig. 1) at the APS beamline. The main component of the optics stage assembly is the Physik Instrumente (PI) XYZ nanopositioning stage, which carries the zone plate focusing optics attached to the zone plate holder, is bolted to the aluminum alloy reference frame. The displacement of the XYZ nanopositioning optics stages (and sample stages) is measured by high-precision Attocube laser interferometric sensors. Laser from the standard Attocube collimating sensor heads is back reflected from mirrors glued on the zone plate holder. The optics fine scanning, closed-loop control system is comprised of PI XYZ fine scanning stages, National Instruments (NI) control hardware, and Attocube laser interferometric displacement sensors. The NI control hardware includes a NI cRIO-9039 real-time controller with a Kintex-7 325T field-programmable gate array (FPGA) built into the chassis, NI-9402 digital input–output (DIO) modules, and NI-9263 analog voltage output modules. The zone plate optics XYZ stage displacement is measured by high resolution Attocube laser interferometric sensors. A total of three sets of quadrature signals representing the position information along each stage axes are generated by the Attocube hardware. These are then read through the NI-9402 DIO modules directly into the Kintex-7 FPGA in the NI cRIO chassis. The reference trajectory generation, processing of the stage displacement information from the Attocube sensors, and running of the discrete feedback controller are done in the FPGA at a 25 kHz rate. The controller output voltage is provided by the NI 9263 analog output module. This voltage signal is amplified through a predefined scaling factor in the PI amplifier designed to work with the PI XYZ optics scanning stages. The amplified voltage signal goes to the piezoactuators of the PI XYZ stages and actuates the stages to move to commanded position in the three-dimensional Euclidean space.

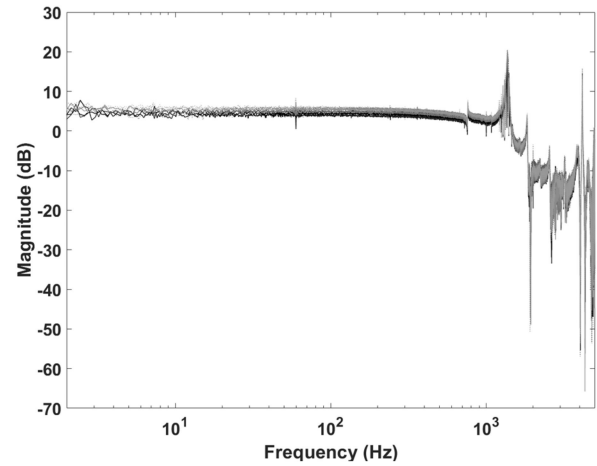


Fig. 3. Nine different nonparametric transfer function estimates calculated by Welch's method for X-stage identification. Here, X-stage means a model between X-stage input signal and X-stage output signal. Similar estimates were obtained for Y- and Z-stages.

III. EXPERIMENTAL SYSTEM IDENTIFICATION

The PI parallel kinematics fine positioning XYZ stages are too complex to model from first principles. Therefore, we used frequency-response-based identification to model the stage dynamics, where at each operating point, a transfer function estimated from the input–output experimental data. More specifically, the response (as determined from Attocube sensor measurement) of each axis to an input of band-limited white noise (0–12 kHz, 5 nm amplitude) was acquired, and a frequency response function (FRF) was estimated from the input–output time-domain data. The frequency components of the input band-limited white noise signal included our frequency range of interest (0–1 kHz) plus additional bandwidth beyond the operational frequency range of the device, such that any out-of-range dynamics that contribute to in-range response could be revealed. The amplitude of the white noise is chosen to be a small value so as not to overexcite the stages at their respective natural frequencies. The stages are excited for over 6 min at 25 kHz rate while simultaneously collecting the stage input–output data during each identification experiment. A transfer function was estimated from input–output data by Welch's method to generate a nonparametric model and another model was fit to the nonparametric model.

To assess nonlinear behavior of the stages we studied the differences in the frequency responses estimated at various operating points. Note that for an ideal linear system, the frequency response data would be independent of the operating point. Accordingly, FRFs were obtained for multiple X-stage dc offsets (−6000, 0, and 6000 nm), Y-stage dc offsets (−2000, 0, and 2000 nm), and Z-stage dc offsets (−6000, 0, and 6000 nm), respectively, for a total of nine measurements for each stage (Fig. 3). Small variations mainly in the high frequencies are observed for X-stage. Similar transfer function estimates were obtained for Y- and Z-stages.

Fig. 3 shows that X-stage dynamics are well approximated by linear models, with the variations being viewed as a perturbation

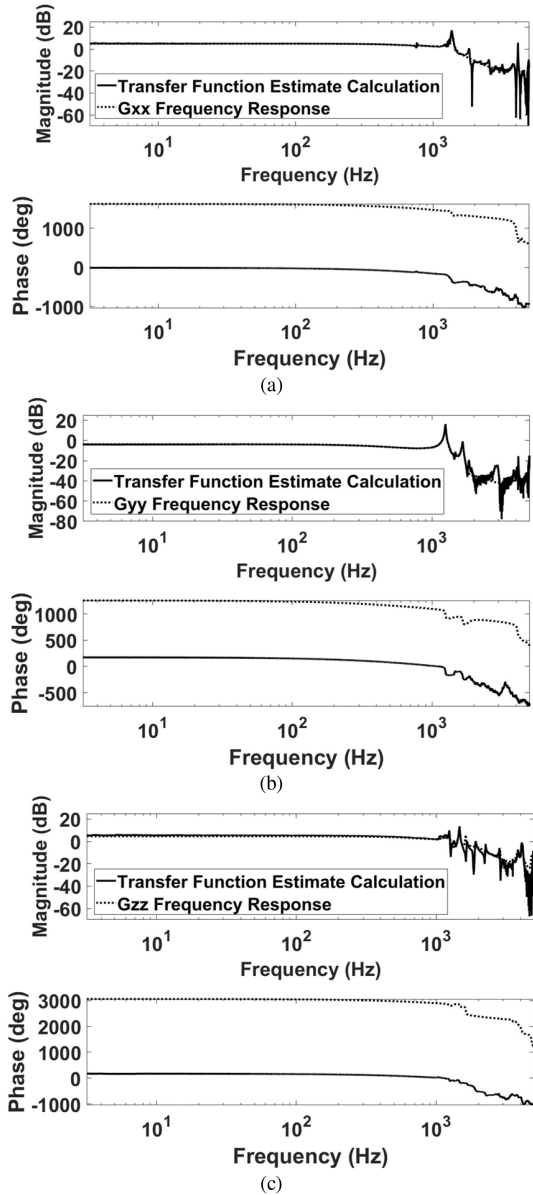


Fig. 4. Comparison between the transfer function estimate calculation of the experimental FRF of Velociprobe fine scanning stages and the frequency response of the corresponding fitted models. (a) 15th-order fitted model G_{xx} , (b) 13th-order fitted model G_{yy} , and (c) 33rd-order fitted model G_{zz} .

of the nominal linear models. Similar results were obtained for the Y- and Z-stages. The linear control design methodology will account for the perturbed linear models by incorporating feedback laws with high gains on the frequency range of operation, making the system insensitive to variations in the plant in these frequencies. After estimating the FRFs at each operating point, the average of the nine FRFs was calculated for each of the X-, Y-, and Z-stages. Transfer functions were then fit to each of the three averaged FRFs; more specifically, 15th, 13th, and 33rd-order transfer functions G_{xx} , G_{yy} , and G_{zz} were fit to model X-, Y-, and Z-stage dynamics, respectively (Fig. 4). The first resonant peaks for X, Y, and Z fine positioning optics stage are at 1.3, 1.2, and 1.2 kHz, respectively.

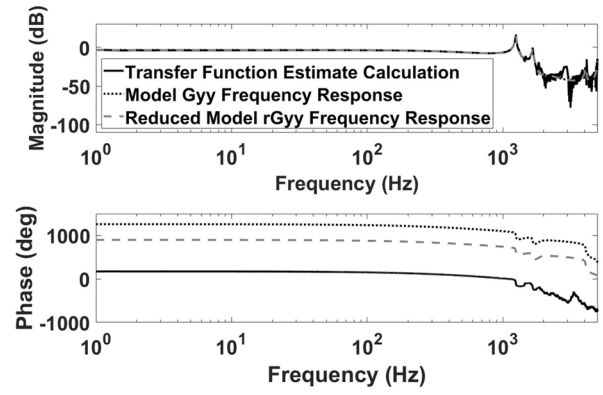


Fig. 5. Comparison between the transfer function estimate calculation of the experimental FRF of Y-stage and the frequency response of the fitted model G_{yy} (13th order) and reduced fitted model rG_{yy} (12th order).

Stage model order was reduced for the ease of control design and implementation, while ensuring the reduced model captured the dynamics of the fit model in frequency band of interest. We used a balanced realization [26] of the stage model transfer functions, where it is easy to quantify the extent of observability and controllability of each state of the stage model. This enables a significant model reduction by removing the barely observable or controllable states [26]. Fig. 5 compares Y-stage averaged experimental FRF, the stage model G_{yy} and the reduced stage model rG_{yy} .

IV. CONTROL DESIGN

A. Control Objectives, Limitations, and Tradeoffs

The identified plant models (as presented in the previous section) were used to design two different control algorithms. First, a conventional PID controller was designed. The PID controller was designed based on the experimentally identified scanning stage models. The PID tuning was done using MATLAB and Simulink control systems toolbox to achieve maximum bandwidth possible. Designed PID controller performance was verified through simulations done in Simulink with reference tracking with added noise and then implemented on the FPGA hardware. PID design is found in current X-ray microscopes and established a baseline for performance comparison. Next, a H_∞ controller was designed using an optimal control design framework that incorporated performance objectives. Both the X and Y fine stage models exhibit nonminimum phase zeros, which impose fundamental constraints on control design [26]. One limitation, being the achievable closed-loop tracking bandwidth that cannot be overcome regardless of the control design. In this article, designs are developed that achieve prespecified tradeoffs between tracking bandwidth, positioning resolution, and robustness to modeling uncertainties.

Velociprobe positioning system is represented in Fig. 6, where, G is the identified model of scanning X, Y, or Z stage, and \hat{G} represents the dynamics of the Velociprobe between the piezoactuator voltage input u and the stage displacement y , including any contributions to those dynamics from the other

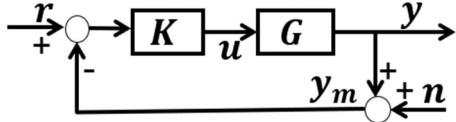


Fig. 6. Closed-loop block diagram. Here, n and r are the measurement noise and reference signals.

fine stage, coarse stages, and the laser interferometer sensors. For each stage, the feedback-control-based architecture (Fig. 6) uses the stage displacement measurement $y_m = y + n$, to reduce the tracking error $e = r - y$ and address other performance objectives. The tracking error $e = Sr + Tn$ and the control effort $u = KSr - KSn$, where, $S = 1/1 + GK$ and $T = GK/1 + GK$, respectively, represent the closed loop sensitivity and complementary sensitivity transfer functions. The control design objectives and fundamental performance limitations can be quantified in terms of these expressions; the controller K should be such that the $|S(j\omega)|$ is small at frequencies ω corresponding to tracking bandwidth, where reference signal r is prominent, and such that $|T(j\omega)|$ is small at high frequencies where noise n is prominent, for better noise attenuation and high positioning resolution. Such a control design will ensure that tracking error e is small at all frequencies. Similarly designing K such that $|K(j\omega)S(j\omega)|$ is small at the frequencies up to the tracking bandwidth ensures that control effort u is sufficiently small, and therefore implementable. There are certain fundamental limitations that cannot be overcome regardless of the control design K ; for instance, note that algebraically $S(j\omega) + T(j\omega) = 1$ regardless of the choice for K ; therefore $|S(j\omega)|$ and $|T(j\omega)|$ cannot simultaneously be made small at a frequency ω . Thus, if noise n has large components in a frequency range of γ within the desired closed-loop bandwidth, then it is not possible to simultaneously achieve large tracking bandwidth and good positioning resolution in that range. It then becomes necessary to design controllers to achieve a tradeoff [25], [27] between better tracking bandwidth or high-positioning resolution objectives. Considerate tuning of design parameters to achieve stabilizing controllers that can be implemented with chosen design objectives is required, all the while keeping γ small.

PID controllers were designed and used to establish the baseline performance of the fine positioning stages. The most common trajectory for the zone plate fine positioning stages is a raster scan. As such, a PID controller becomes particularly attractive as compared to open loop because of the capability to track ramp signals with zero steady-state error due to the integral action. Since PID implementations are low-order designs they are not flexible enough to simultaneously accommodate multiple design objectives such as tracking bandwidth, positioning resolution, and robustness.

B. H-Infinity Controller Design

In our work, we use the H_∞ control design architecture, where we pose an optimization problem that incorporates simultaneously the design objectives of large tracking bandwidth, high-positioning resolution, bounded control effort, sufficient

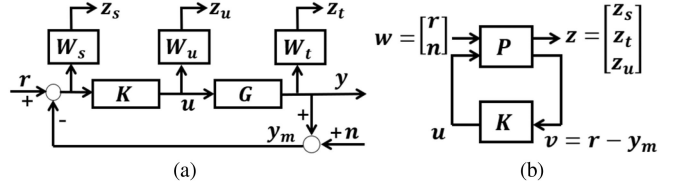


Fig. 7. Closed loop transfer function block diagrams for the S\TKS mixed-sensitivity minimization problem. (a) Closed loop system with the identified plant model G , reference r , plant input u , measurement noise n , design weights W_s , W_t , and W_u and regulated outputs, z . (b) Generalized plant framework with the transfer function going from exogenous inputs w to regulated outputs z to be minimized to achieve the optimum control law K .

environmental disturbance rejection, and attenuation of measurement noise. The optimization problem formulation can be easily explained in terms of the closed-loop system shown in Fig. 7. Here G represents an identified model of the X-, Y-, or Z-stage, y is the corresponding stage displacement, and y_m is the displacement measured by the laser interferometer sensor that includes the measurement noise n . In the optimization problem, the signals of interest are the weighted tracking error $z_s = W_s(r - y)$ reflecting the tracking bandwidth objective, the weighted displacement $z_t = W_t y$ reflecting the noise attenuation objective, and the weighted control effort $z_u = W_u u$ reflecting control effort bound objective. To obtain the controller K an optimization problem is posed as follows:

$$\inf_K \|T_{wz}\|_\infty \quad (1)$$

$$T_{wz} = [W_s S, -W_s S; W_t T, -W_t T; W_u K S, -W_u K S]^T \quad (2)$$

where T_{wz} (2) is the matrix transfer function from $w = [r \ n]^T$ to $z = [z_s \ z_t \ z_u]^T$ and operation $\|\cdot\|_\infty$ denotes the H_∞ norm.

In practice, solving the optimization problem for a suboptimal controller is much easier than solving for an optimal controller. If γ_{optimal} represents the optimal value (minimum) of the H_∞ -norm of the closed loop transfer function matrix, then a suboptimal $\gamma > \gamma_{\text{optimal}} > 0$ is chosen [26]. The value of γ increases as a result of accommodating better tracking bandwidth or high-positioning resolution objectives. Considerate tuning of design parameters to achieve stabilizing controllers that can be implemented with chosen design objectives is required, all the while keeping γ small.

The weighting transfer function W_s influences the tracking error and tracking bandwidth. W_s is designed as a low-pass filter with large magnitude over the desired tracking bandwidth; this ensures that the optimal controller K resulting from (1) is such that the transfer function S is small over the bandwidth. This design enforces a lower bound to the achievable closed-loop bandwidth ω_B [26]. Typically, the bandwidth of the closed-loop system is usually defined by the -3 dB bandwidth, which is the minimum frequency at which the magnitude $|S(j\omega)|$ becomes greater than -3 dB (note that -3 dB $\approx 70\%$ amplitude). Thus, an X-ray microscope scanner with a -3 dB bandwidth of ω_B Hz implies that the magnitude of tracking error is smaller than 70% of the magnitude of reference signal when its frequency

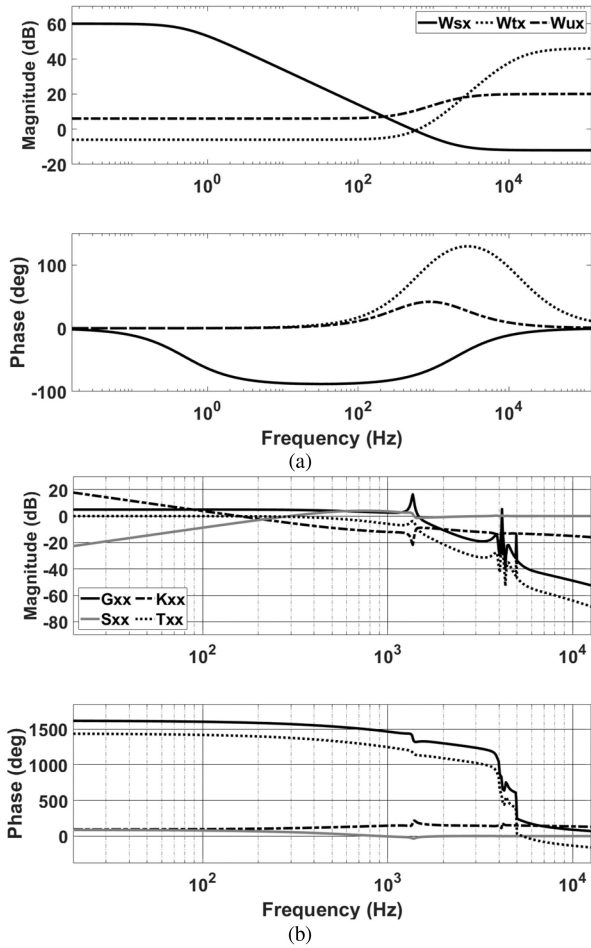


Fig. 8. Bode plot of (a) weighting transfer functions W_{sx} , W_{tx} , and W_{ux} for the X-stage corresponding to the H_∞ controller with -3 dB bandwidth of 200 Hz; (b) stage model G_{xx} , controller K_{xx} , design sensitivity and complementary sensitivity S_{xx} and T_{xx} .

components are within ω_B Hz. In this article, we will define analogously -40 dB bandwidth instead as a measure of bandwidth (note -40 dB = 1%). In the case of the Velociprobe optics fine positioning X-stage the largest -3 dB bandwidth of 200 Hz was achieved. Accordingly, $W_{sx} = (0.25 s + 3142)/(s + 3.142)$, a low-pass filter was designed [Fig. 8(a)]. The weighting transfer function W_t influences high-frequency noise attenuation. W_t is designed as a high-pass filter with large magnitudes at high frequencies (beyond desired tracking bandwidth). This results in transfer function $T = GK/(1 + GK)$ to roll off beyond the crossover frequency ω_T , and thus attenuating the noise effects beyond this frequency. Accordingly, the complementary sensitivity weight $W_{tx} = \frac{s^2 + 7997s + 1.59 \times 10^7}{0.005 s^2 + 799.7 s + 3.198 \times 10^7}$ was chosen to be a second-order high-pass filter [Fig. 8(a)]. The positioning resolution of a scanner, considered to be the smallest realizable displacement, is defined as three times standard deviation (3σ) of the scanner motion measurements when the reference signal is zero. In our experiments, we determined 3σ of scanner displacement over a long time (over 5 min at 25 kHz sampling rate). Note that the scanner displacement is given by $y = Tn$ when the reference $r = 0$. In general, displacement sensor noise is introduced into the system at high frequency, so designs with

smaller ω_T (lower roll-off frequencies for T) and with a higher roll-off rate (that is steeper slope for $|T(j\omega)|$ for $\omega > \omega_T$) result in higher positioning resolution. The control effort weighting function W_u influences the size of the KS transfer function by placing an upper bound on it to bound the control effort, in low frequencies up to the bandwidth frequency to counter any saturation. For frequencies after the bandwidth frequency the KS transfer function was designed to decay and bounded within a smaller value. Control effort weighting transfer function for the X-stage $W_{ux} = (10 s + 2.513 \times 10^4)/(s + 1.257 \times 10^4)$ is shown in Fig. 8(a). The H_∞ controller K_{xx} designed with these design weights and the corresponding closed loop transfer function are shown in the Bode plot in Fig. 8(b). Similarly, for the Y- and Z-stages, the highest -3 dB bandwidth achieved with H_∞ control design is 200 Hz (150% improvement over PID controller) and 200 Hz (132% improvement over PID controller), respectively.

V. IMPLEMENTATION

The designed controllers were implemented on the NI cRIO control hardware described in Section II. PID controllers are of lower order (second order) transfer functions. In contrast, the controller transfer functions designed by the H_∞ -framework were of higher orders (order 10–30). The existing function blocks in the LabVIEW software libraries are inadequate for implementation of these controllers due to limitations such as maximum controller order representable, unsatisfactory performance with higher order controllers, maximum achievable sampling frequency, and inadequate predefined coefficient precision. To resolve the implementation issues in FPGA the discretized controllers were represented by biquad structure [28] represented as $H(z) = R_0 \prod_q \frac{1+b_{1q}z^{-1}+b_{2q}z^{-2}}{1+a_{1q}z^{-1}+a_{2q}z^{-2}}$, where, z^{-1} is the delay, R_0 is gain, and q is number of second-order transfer function (second-order sections) in the structure. In the Xilinx Kintex-7 7K325T FPGA that was used, only three second-order sections could be accommodated in series before exhausting all the FPGA resources. The remaining resources in the FPGA was required for generating reference, post processing measured displacement and running the controller algorithm. This made it possible to successfully implement all PID controllers and any controller with order up to six. To implement high-order controllers with the limited available FPGA resources a single second order section block was recursively used in a loop to represent the whole controller transfer function. So now a 20th-order H_∞ -controller transfer function can be implemented using one second-order section, which requires only one-tenth of the resources. As an extension to this resource allocation technique multiple controllers were represented and implemented in experiment just by using one second-order section block. The recursive utilization structure of available FPGA resources made it possible to implement arbitrary order controller.

VI. EXPERIMENTAL RESULTS

For the zone plate fine positioning X-stage the maximum -3 dB bandwidth of 149 Hz and -40 dB bandwidth of 2.0 Hz was achieved with a second-order PID controller after an

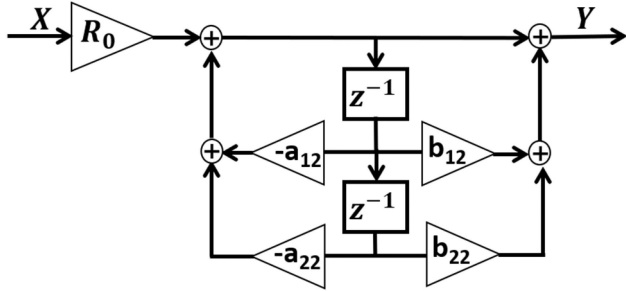


Fig. 9. Block diagram of a second-order section or biquad structure.

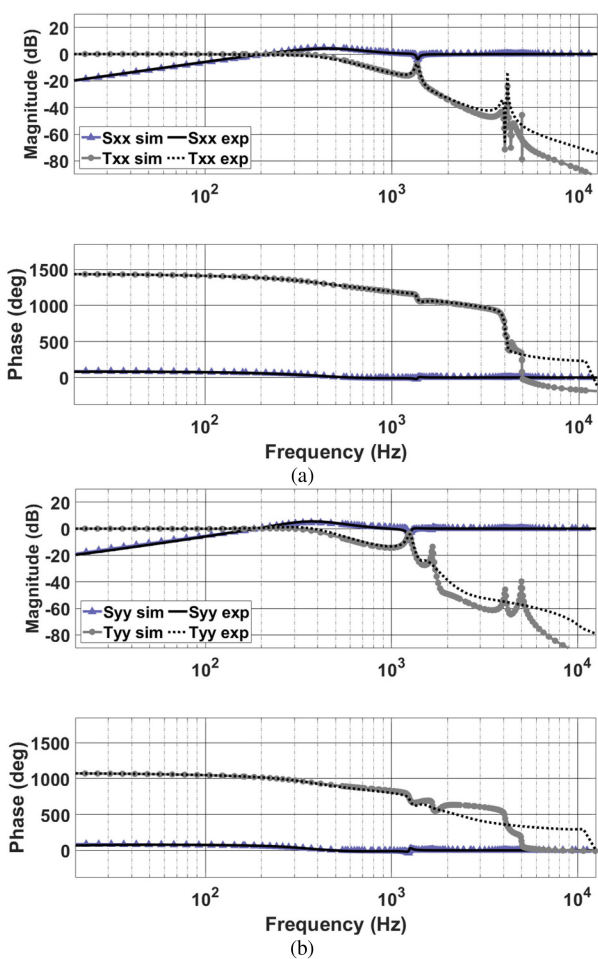


Fig. 10. Experimental verification of closed loop transfer function S and T for X-stage (a) PID, and (b) H_∞ .

exhaustive search over design parameters. Experimental closed-loop transfer functions $S_{xx,\text{exp}}$ and $T_{xx,\text{exp}}$ were identified from the experimental closed-loop data using black-box identification and compared to design $S_{xx,\text{sim}}$ and $T_{xx,\text{sim}}$, where, G_{xx} is the identified X-stage model (15th order) and $K_{PID,xx}$ is the PID controller. Fig. 10(a) shows that experimentally identified design sensitivity transfer function $S_{xx,\text{exp}}$ is a good match with the $T_{xx,\text{exp}}$ matches the design $T_{xx,\text{sim}}$ up around 100 Hz [Fig. 10(a)] and then shows a similar downward trend in higher frequencies.

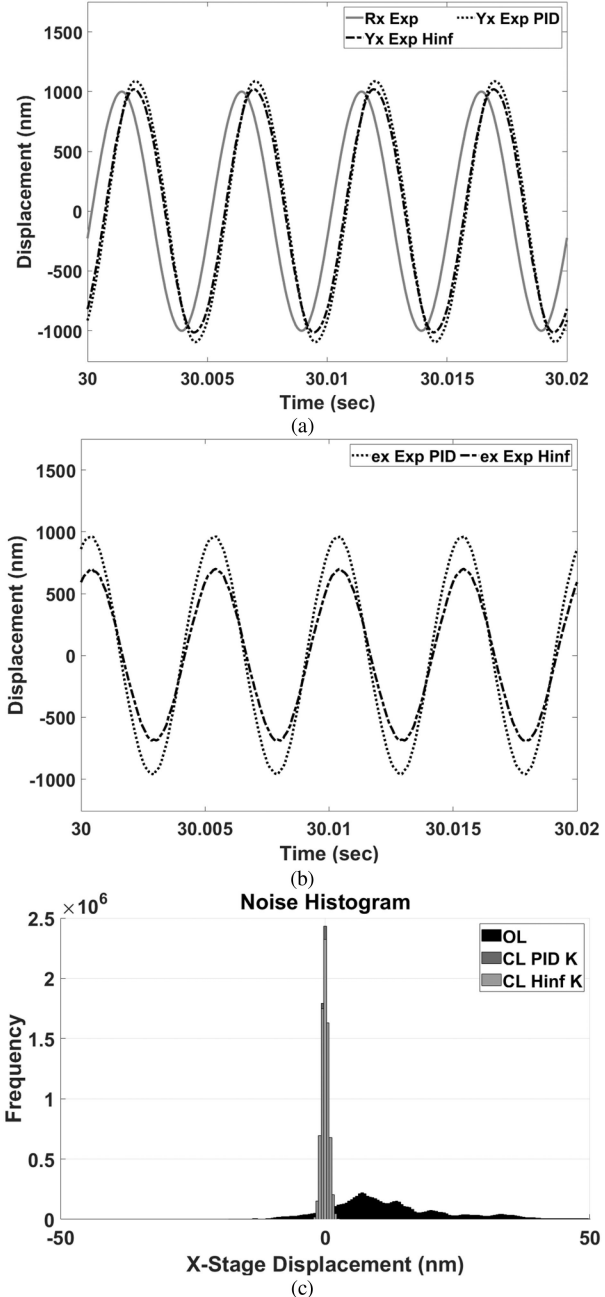


Fig. 11. (a) Experimental closed loop X-stage tracking verification of a PID and a H_∞ -controller with 149 and 200 Hz bandwidth, respectively. (b) Tracking error comparison. (c) Noise histogram for the X-stage in open loop, PID, and H_∞ -controller.

In the case of the H_∞ -controller K_{xx} for fine scanning X-stage the maximum -3 dB bandwidth achieved is 200 Hz and -40 dB bandwidth of 2.6 Hz, which is a 134% and 130% improvement design sensitivity $S_{xx,\text{sim}}$ corresponding to $K_{PID,xx}$. Similarly, on -3 dB and -40 dB bandwidth, respectively, over the baseline PID controller. Experimentally identified closed-loop transfer functions show a close match with design S and T [Fig. 10(b)]. Fig. 11 compares closed-loop tracking performance between the PID (149 Hz bandwidth) and H_∞ (200 Hz bandwidth) designs. Fig. 11(b) shows the tracking error comparison between (PID

and H_∞ controller with the reference signals being a sine wave (amplitude 1000 nm and frequency 200 Hz). The tracking errors for the PID and h-inf controllers are, respectively, around 1000 nm and 650 nm. This shows the H_∞ design is performing significantly better than the PID. The noise histograms in Fig. 11(c) were obtained from separate noise experiments in open loop, with PID, and with H_∞ controller. In the noise experiments zero input was given to the system and the output (stage displacements) were measured. These experimental nonzero outputs correspond to effects of system noise. The noise histograms [Fig. 11(c)] shows the spread of open-loop stage output is large and not zero mean due to presence of open-loop stage drift. Both PID and H_∞ -controller completely removes the effect of drift and has a less spread resulting in better positioning resolution. The 3σ positioning resolution achieved by the H_∞ -controller is 1.9 nm (same as PID) which is over 16-times improvement over open-loop positioning resolution of 33 nm. The H_∞ -controller was designed with a large bandwidth objective in mind, which resulted in the positioning resolution same as that of PID controller.

For the Y-stage PID controller design resulted in maximum -3 dB bandwidth of 134 Hz and -40 dB bandwidth of 1.7 Hz. In comparison, with H_∞ design -3 dB bandwidth of 200 Hz and -40 dB bandwidth of 2.7 Hz (150% and 158% improvement, respectively) compared to baseline PID controller. The experimental closed-loop transfer functions were verified as in Fig. 12. Improved tracking performance is achieved with H_∞ compared to PID design as shown in Fig. 13(a) and (b). H_∞ controller showcases a 3σ positioning resolution of 1.4 nm (like PID) both resulting in significantly better positioning resolution than the open loop (12 nm), shown in Fig. 13(c).

VII. X-RAY PYCHOGRAPHIC IMAGING WITH VELOCIPROBE

A. Step-Scan Imaging

In step-scan X-ray imaging, first the X-ray beam is focused on to a spot on the sample and the corresponding diffraction pattern is collected at the detector downstream of the sample. Then, the X-ray spot is moved to the next location with a predefined horizontal and/or vertical step size which needs to be smaller than the spot size to obtain overlap between scan points. A settling time is allowed for the optics scanning stages to reach the second location, before another diffraction pattern is recorded for a predefined exposure time. In the experiment, X-rays with a photon energy of 7.5 keV were focused by a Fresnel zone plate with the outmost zone width of 50 nm, a gold Siemens star test pattern with 30 nm finest spokes was placed around the focus point with an illumination spot size of about 80 nm. A $9 \mu\text{m}^2$ area was scanned using the step-scan technique in the following three modes.

- 1) Mode-1: Open loop – zone plate motion only.
- 2) Mode-2: Closed loop – zone plate motion only.
- 3) Mode-3: Closed loop – differential motion.

In all modes the sample stage remains fixed, the zone plate was moved in a raster-scan pattern with a step size of 20 nm for both X- and Y-direction and diffraction patterns were acquired by a Dectris Pilatus 300 K detector with an exposure time of about

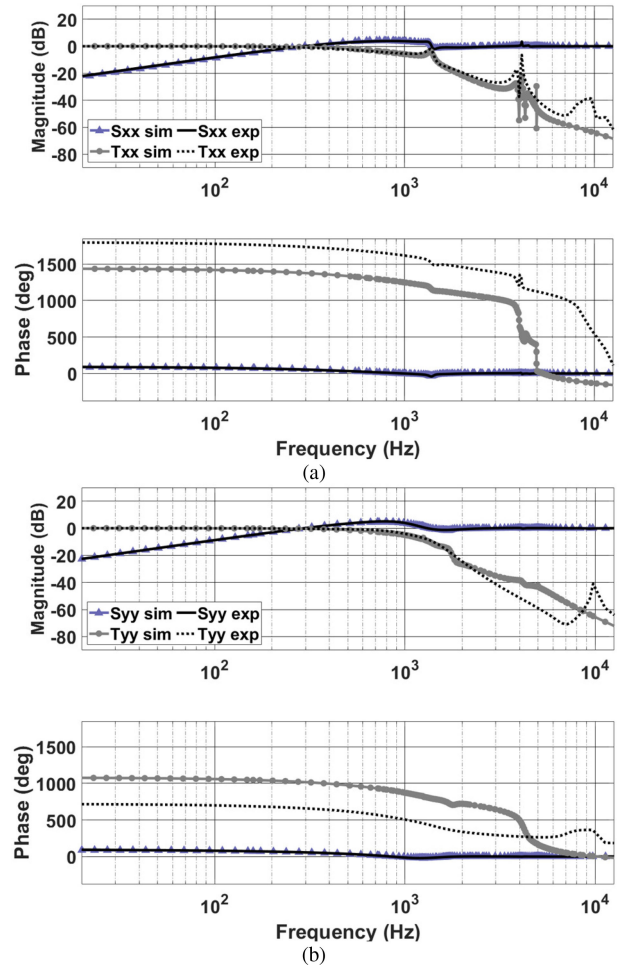


Fig. 12. Experimental verification of closed loop transfer function S and T for Y-stage (a) PID, and (b) H_∞ -controller.

50 ms. Each of the step scans took about 75 min, of which 75% of the experiment time was spent on the scan overhead. 256×256 pixels of each diffraction pattern were cropped for the ptychographic reconstruction using a custom software package [13], yielding an image pixel size of 6.7 nm (Fig. 14).

In the Mode-1, the sample stage remains fixed, the zone plate optics stage scans the predefined area on the sample following the raster scan trajectory in open loop (no controllers). The recovered phase image in Fig. 14(a), which is skewed, and the circular patterns are appearing like ellipsoids, the features are not that straight and there is edge ambiguity of the straight features. Fig. 14(b) is the phase image for Mode-2 (the H_∞ -controllers are engaged). With better positioning accuracy of the zone plate stages using H_∞ -controllers, the X-ray image quality has improved, it shows circular rings and clear spokes. However, some spokes are still distorted and twisted with some edge ambiguity that mainly results from the relative drift between the sample and zone plate during the long scan. The Mode-3 is where the zone plate optics stages tracks both reference trajectory and the sample stages (to counter the drift of sample stages) in closed loop with the H_∞ controllers. As a result, the relative drift between the optics stage and sample stage is minimized in closed

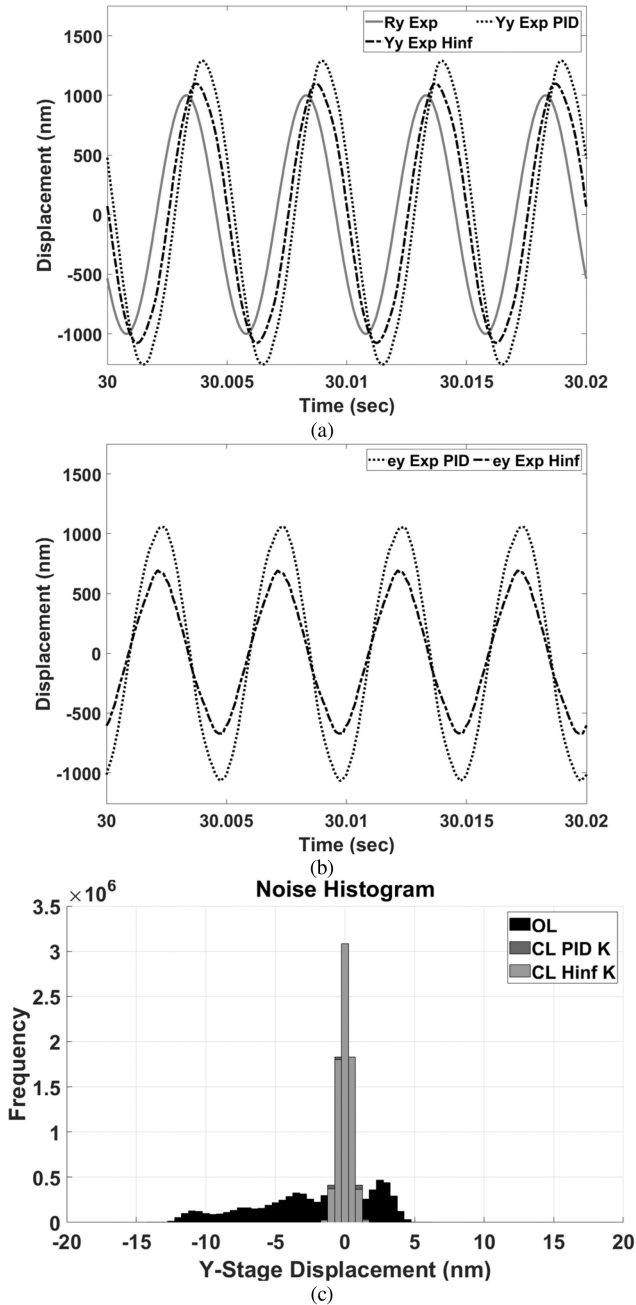


Fig. 13. Experimental closed loop Y-stage tracking verification of a PID and a H_∞ -controller with -3 dB bandwidth of 134 and 200 Hz, respectively. (b) Tracking error comparison. (c) Noise histogram for Y-stage in open loop, PID, and H_∞ -controller.

loop. **Fig. 14(c)** is the ptychographic image for the Mode-3 and is much better than that observed with the other two cases, with the spokes well recovered and finest features (30 nm) resolved.

B. Flyscan Imaging

In the flyscan technique [13], the optics scanning stages continuously tracked a predefined trajectory to scan the X-ray spot and cover the region of interest of the sample while the diffraction patterns were simultaneously collected at the area detector downstream of the sample. The square snake scan

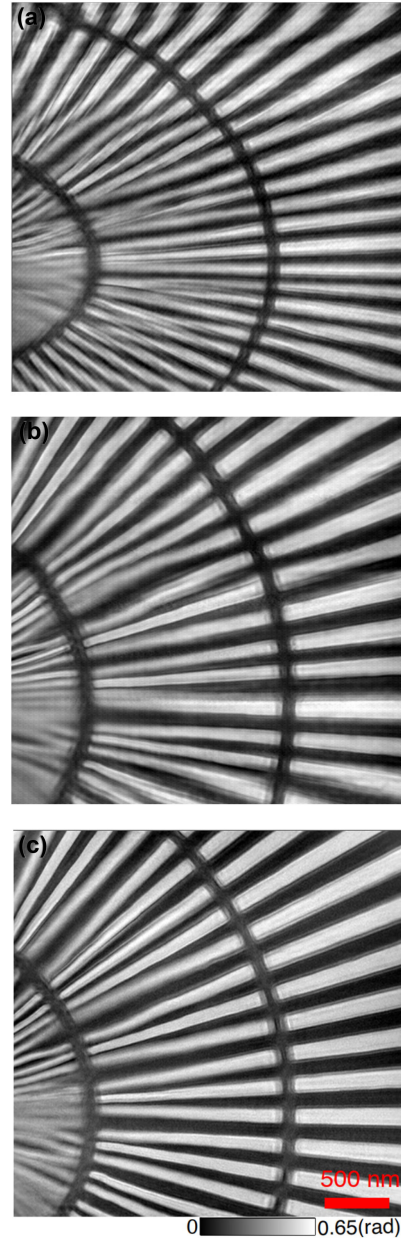


Fig. 14. Step-scan ptychography reconstructed phase image of a Siemens Star pattern by (a) open loop – zone plate motion only, (b) closed loop – zone plate motion only with the H_∞ -controllers in diagonal, and (c) closed loop – differential motion with the H_∞ -controllers in diagonal.

trajectory is a custom trajectory generated in the FPGA that incorporates custom scan area, horizontal and vertical step size, and has a custom scanning speed directly tied to the detector trigger frequency. Flyscan enabled the scanning of a $1 \mu\text{m}^2$ area in 0.01 s compared to 4.5 s required for step scan using same scan parameters on same area (450-times improvement). The X-ray images in **Fig. 15** show the comparison of the PID and H_∞ controllers in flyscan technique with detector trigger frequency being 3 kHz. The phase images obtained by ptychography reconstruction show similar performance for PID and H_∞ -controller. The reason behind this stems from the combined effect of the custom square snake scan trajectory and ptychographic X-ray

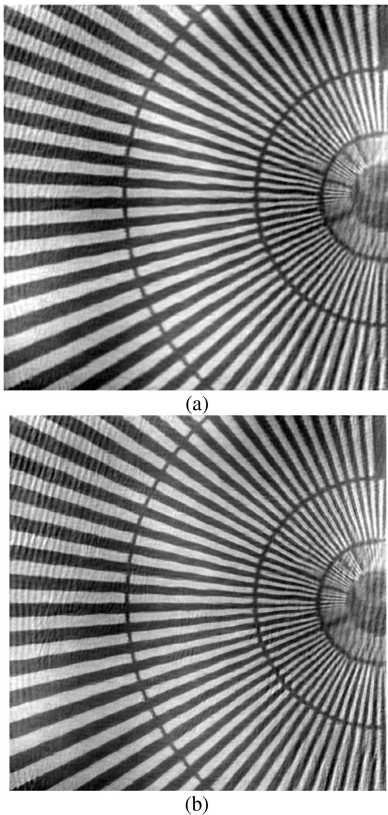


Fig. 15. Flyscan X-ray ptychographic image of a Siemens Star in closed loop (a) PID and (b) H_∞ controller.

imaging technique. First, the square snake scan trajectory has long straight segments ($9 \mu\text{m}$) with small vertical jumps to the next line at the end of each line, making it easy to track. Second, in the ptychographic imaging the probes have horizontal and vertical overlap of 66% and 50%, respectively, resulting in a lot of redundant information. Choice of detector trigger signal (square wave generated in FPGA) with very high duty cycle (up to 99.5%), custom trajectory, large probe overlaps, and continuous data collection by detector helps ptychographic reconstruction work good for both PID and H_∞ controllers. The benefit of H_∞ controller will be in experiments with larger bandwidth requirement, trajectory with lot of curves (spiral, circular, and Lissajous) and ultrafast detector (up to 5–6 MHz). Even then the images obtained using H_∞ design are sharper than that of PID.

VIII. CONCLUSION

This article presented the design and implementation of PID and one degree of freedom H_∞ -controllers for Velociprobe X-ray microscope at APS. Conventional PID controllers helped achieve -3 dB bandwidths of 149, 134, and 151 Hz for the X-, Y-, and Z-stages, respectively. The H_∞ -control design was shown to accommodate the performance specifications such as tracking bandwidth, positioning resolution, disturbance rejection, measurement noise, and robustness to unmodeled dynamics. The H_∞ control laws when implemented results in

a -3 dB bandwidth improvement of 134% (200 Hz), 150% (200 Hz), and 132% (200 Hz) for X-, Y-, and Z-stages over PID controllers, respectively. Another significant contribution is using the biquad structure implement the discrete controllers. Two scanning techniques, step scan and flyscan, for X-ray ptychographic imaging with the Velociprobe X-ray microscope are presented. The step scan results show that the differential close-loop control between the sample and optics can compensate the relative drift – a enabling feature for which is high-resolution ptychography and long run-time imaging. With the flyscan technique, we demonstrated an imaging rate of 0.01 seconds per square microns, which is 450-times faster than a step scan with the same scan parameters. This performance can be further improved upon by augmenting the proposed feedback control with feedforward control [18] and methods such as iterative learning control [15], [17], [24]. In [1], we augmented this optimal control architecture with a design for countering sensor drift in real time through drift measurements.

ACKNOWLEDGEMENT

The authors would like to thank the support, help, and discussion with P. Hartog, S. Vogt, J. Maser, C. Roehrig, Z. Cai, B. Lai, S. Sullivan, and D. Vine.

REFERENCES

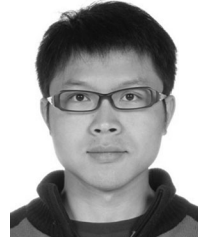
- [1] S. T. Mashrafi, C. Preissner, and S. M. Salapaka, “Sensor drift rejection in X-ray microscopy: A robust optimal control approach,” in *Encyclopedia of Systems and Control*, London, U.K.: Springer, 2019.
- [2] C. Preissner *et al.*, “Earth, wind, and fire: The new fast scanning Velociprobe,” in *Proc. 9th Mech. Eng. Des. Syn. Rad. Equ. Instrum. Conf.*, 2017, pp. 1–4.
- [3] J. Deng *et al.*, “The Velociprobe: A fast hard X-ray nanoprobe for ptychographic imaging,” in *Proc. SPIE, X-Ray Nanoimaging Instrum. Methods III*, 2017, vol. 10389, pp. 112–115.
- [4] S. T. Mashrafi, C. Preissner, and S. M. Salapaka, “The Velociprobe: Pushing the limits with fast and robust control,” in *Proc. 32nd Annu. Meeting Amer. Soc. Precis. Eng.*, Feb. 2017, pp. 468–473.
- [5] S. T. Mashrafi, C. Preissner, and S. M. Salapaka, “Fast scanning of X-ray optics: An optimal control approach,” in *Proc. 31st Annu. Meeting Amer. Soc. Precis. Eng.*, 2016, pp. 97–102.
- [6] C. Lee and S. M. Salapaka, “Model based control of dynamic atomic force microscope,” *Rev. Sci. Instrum.*, vol. 86, no. 4, pp. 043703-1–043703-8, 2015.
- [7] D. Y. Abramovitch, “The discrete time biquad state-space structure: Low latency with high numerical fidelity,” in *Proc. Amer. Control Conf.*, 2015, pp. 2813–2818.
- [8] J. Deng *et al.*, “Continuous motion scan ptychography: Characterization for increased speed in coherent X-ray imaging,” *Opt. Express*, vol. 23, no. 5, pp. 5438–5459, 2015.
- [9] E. Nazaretski *et al.*, “Design and performance of scanning ptychography microscope,” *Rev. Sci. Instrum.*, vol. 85, no. 3, pp. 033707-1–033707-5, 2014.
- [10] J. Gofron, *et al.*, “Piezo control for 1 nm spatial resolution synchrotron X-ray microscopy,” *Proc. 17th Pan-Amer. Syn. Rad. Inst. Conf.*, 2014, vol. 493.
- [11] J. Maser *et al.*, “A next-generation hard X-ray nanoprobe beamline for in situ studies of energy materials and devices,” *Metall. Mater. Trans. A*, vol. 45, no. 1, pp. 85–97, 2014.
- [12] M. Borland, “Ultra-low-emittance light sources,” *Synchrotron Radiat. News*, vol. 27, no. 6, p. 2, 2014.
- [13] Y. Nashed *et al.*, “Parallel ptychographic reconstruction,” *Opt. Express*, vol. 22, no. 26, pp. 32082–32097, 2014.
- [14] E. Nazaretski *et al.*, “Performance and characterization of the prototype nm-scale spatial resolution scanning multilayer laue lenses microscope,” *Rev. Sci. Instrum.*, vol. 84, no. 3, pp. 033701-1–033701-7, 2013.

- [15] E. Eleftheriou and S. O. R. Moheimani, *Control Technologies for Emerging Micro and Nanoscale Systems*, Berlin, Germany: Springer, vol. 413, 2011.
- [16] A. Maiden *et al.*, “An improved ptychographical phase retrieval algorithm for diffractive imaging,” *Ultramicroscopy*, vol. 109, no. 10, pp. 1256–1262, 2009.
- [17] B. Helfrich *et al.*, “Combined H_∞ -feedback control and iterative learning control design with application to nanopositioning systems,” *IEEE Trans. Control Syst. Technol.*, vol. 18, no. 2, pp. 336–351, Jul. 2008.
- [18] C. Lee and S. M. Salapaka, “Two degree of freedom control for nanopositioning systems: Fundamental limitations, control design, and related trade-offs,” in *Proc. Amer. Control Conf.*, 2009, pp. 1664–1669.
- [19] P. Thibault *et al.*, “High-resolution scanning x-ray diffraction microscopy,” *Science*, vol. 321, no. 5887, pp. 379–382, 2008.
- [20] S. M. Salapaka *et al.*, “Scanning probe microscopy,” *IEEE Control Syst. Mag.*, vol. 28, no. 2, pp. 65–83, Apr. 2008.
- [21] D. Shu *et al.*, “Optomechanical design of a hard X-ray nanoprobe instrument with nanometer-scale active vibration control,” in *Proc. Ninth Int. Conf. Syn. Rad. Instrum.*, 2007, pp. 1321–1324.
- [22] J. Rodenburg *et al.*, “Hard X-ray lensless imaging of extended objects,” *Phys. Rev. Lett.*, vol. 98, no. 3, pp. 034801–1–034801–4, 2007.
- [23] S. Devasia, E. Eleftheriou, and S. O. R. Moheimani, “A survey of control issues in nanopositioning,” *IEEE Trans. Control Syst. Technol.*, vol. 15, no. 5, pp. 802–823, Sep. 2007.
- [24] D. Bristow, M. Tharayil, and A. Alleyne, “A survey of iterative learning control,” *IEEE Control Syst. Mag.*, vol. 26, no. 3, pp. 96–114, Jun. 2006.
- [25] S. M. Salapaka *et al.*, “High bandwidth nanopositioner: A robust control approach,” *Rev. Sci. Instrum.*, vol. 73, no. 9, pp. 3232–3241, 2002.
- [26] D. McFarlane and K. Glover, “A loop shaping design procedure using H_∞ synthesis,” *IEEE Trans. Autom. Control*, vol. 37, no. 6, pp. 759–769, Jun. 1992.
- [27] G. E. Dullerud and F. Paganini, *A Course in Robust Control Theory: A Convex Approach*, Berlin, Germany: Springer, 1999.
- [28] S. Skogestad and I. Postlethwaite, *Multivariable Feedback Control: Analysis and Design*, Hoboken, NJ, USA: Wiley, 2001.
- [29] S. Mitra, *Digital Signal Processing: A Computer-Based Approach*, 3rd ed., New York, NY, USA: McGraw-Hill, 2006.
- [30] A. Oppenheim and R. Schafer, *Discrete-Time Signal Processing*, 2nd ed., Upper Saddle River, NJ, USA: Prentice Hall, 1998.
- [31] A. Ambardar, *Analog and Digital Signal Processing*, 2nd ed. New York, NY, USA: McGraw-Hill, 1999.



Sheikh T. Mashrafi (Member, IEEE) received the B.S. degree in mechanical engineering from Bangladesh University of Engineering and Technology, Dhaka, Bangladesh, in 2009, the M.S. and the Ph.D. degrees in mechanical engineering from the University of Illinois at Urbana-Champaign, Urbana, IL, USA, in 2013 and 2019, respectively, in collaboration with the Advanced Photon Source (APS), Argonne National Laboratory (ANL), Lemont, IL, USA from 2012 to 2018.

He is currently a Postdoctoral Researcher with APS, ANL, Lemont, IL, USA. His research interests include controls and dynamics, machine learning, X-ray microscope adaptive optics, and high-precision nanopositioning systems.



Junjing Deng received the B.S. degree in applied physics from Nanjing University of Science and Technology, Nanjing, China, in 2008, the M.S. degree in condensed matter physics from Peking University, Beijing, China, in 2011, and the Ph.D. degree in applied physics from Northwestern University, Evanston, IL, USA, in 2016.

He is currently a Staff Scientist with the Advanced Photon Source, Argonne National Laboratory, Lemont, IL, USA.



Curt Preissner received the Ph.D. degree in mechanical engineering from the University of Illinois at Chicago, Chicago, IL, USA, in 2009.

Since 2004, he has been working with the Advanced Photon Source (APS), Argonne National Laboratory, Lemont, IL, USA. The APS is a national synchrotron light source serving thousands of users each year. At the APS, Dr. Preissner designs high-precision X-ray instrumentation and particle accelerator components. His research interests include nanofocusing X-ray microscopes and dynamic testing and simulation of next-generation synchrotron accelerator magnet support systems.



Srinivasa M. Salapaka (Senior Member, IEEE) received the B.Tech. degree in mechanical engineering from the Indian Institute of Technology, Madras, India, in 1995, the M.S. and the Ph.D. degrees in mechanical engineering from the University of California Santa Barbara, Santa Barbara, CA, USA, in 1997 and 2002, respectively.

During 2002–2004, he was a Postdoctoral Associate with the Laboratory for Information and Decision Systems, Massachusetts Institute of Technology, Cambridge, MA, USA. Since January 2004, he is a Faculty Member with the Department of Mechanical Science and Engineering, University of Illinois at Urbana–Champaign, Urbana, IL, USA.

Prof. Salapaka got the NSF CAREER award in the year 2005. He is an ASME fellow since 2015.